Journal of Materials Chemistry

Dynamic Article Links

Cite this: *J. Mater. Chem.*, 2011, **21**, 4393

www.rsc.org/materials

PAPER

Manganite perovskite nanoparticles for self-controlled magnetic fluid hyperthermia: about the suitability of an aqueous combustion synthesis route

Romain Epherre,[a] Etienne Duguet,[a] Stéphane Mornet,[a] Emil Pollert,[b] Stéphanie Louguet,[acd] Sébastien Lecommandoux,[cd] Christophe Schatz[cd] and Graziella Goglio*[a]

Received 17th November 2010, Accepted 17th January 2011
DOI: 10.1039/c0jm03963b

Unaggregated $La_{0.82}Sr_{0.18}MnO_{3+\delta}$ perovskite nanoparticles with a mean crystallite size of 22 nm were successfully synthesized through an aqueous combustion process (Glycine Nitrate Process, GNP) which takes advantage of exothermic, fast and self-sustaining chemical reactions between metal nitrates and glycine as a suitable organic reducing agent. The influence of *G*/*N* molar ratio on the phase purity, crystallite size and manganese valency was screened. Fuel-rich conditions were selected to improve chelation of the cations in acidic pH and ensure an accurate control of the cationic composition. Fast calcination was optimized to enhance crystallinity of the nanoparticles and subsequent milling step was performed to favour their desaggregation. The manganite nanoparticles were thoroughly characterized by X-ray diffraction (XRD), elemental chemical analysis, Mohr salt titration and transmission electron microscopy (TEM). According to a process derived from the Stöber's method, they were uniformly coated with a 5 nm thick silica shell, as evidenced by TEM, infrared spectroscopy, ζ potential measurements and dynamic light scattering experiments. Preliminary heating experiments in a ac magnetic field showed these core@shell nanoparticles fulfill the requirements for self-controlled magnetic fluid hyperthermia, considering their size (20–70 nm) and their maximum heating temperature (43 °C) which is controlled by the Curie temperature of the magnetic cores.

Introduction

In oncology there is a continuous increase of interest for hyperthermia mostly as a complementary route to chemotherapy and radiotherapy.[1–6] The concept of hyperthermia is based on the higher heat-sensitivity of tumour cells. So, treating tumour regions at temperatures between 41 and 47 °C allows to destroy tumour cells and to spare the healthy ones. Magnetic fluid hyperthermia (MFH) is a promising hyperthermia modality which takes advantage of the capacity of magnetic nanoparticles to convert into heat the energy absorbed from a high-frequency magnetic field, mostly *via* magnetic losses. The clinical protocol would consist in the administration of the stable and non-toxic aqueous suspensions of the magnetic nanoparticles followed by a short-time exposure to ac magnetic fields. The main claimed requirements are a high specific absorption rate (SAR) value of the magnetic suspensions—for minimizing the dose to administer—and a small hydrodynamic size of the colloidal mediators—for a safe systemic use.

Until the last decade, magnetite Fe_3O_4 and maghemite γ-Fe_2O_3 were preferred for the MFH development because of their inherent biocompatibility, their easy synthesis in the form of stable aqueous magnetic fluids and their parallel development as contrast agents in magnetic resonance imaging.[7] That is why the majority of *in vitro* and *in vivo* experiments on animals, and very recently on humans,[8–10] are running with heat mediators based on magnetite or maghemite cores. However, their use is associated with a main inconveniency which concerns the control of the *in vivo* temperature, because not only the heat conduction and energy adsorption *in vivo* are insufficiently known but also local overheating may damage healthy tissue.

For overcoming this issue, a first way is to continuously monitor the temperature distribution for an automatic feedback control of the ac magnetic field output.[8] Unfortunately, conventional thermometry is invasive, especially as the temperature must be taken at several places. A second way could exploit the temperature dependence of the magnetic properties.[4] Actually, Curie temperature T_C is the temperature above which ferromagnetic materials lose their strong magnetic properties and become paramagnetic. So, by designing magnetic nanoparticles with a T_C in the range of the therapeutic temperature (41–47 °C), the heating would spontaneously stop as soon as the environment temperature would reach the T_C value. So, the

[a]*CNRS, Université de Bordeaux, ICMCB, 87 avenue du Dr Albert Schweitzer, F-33608 Pessac, France. E-mail: goglio@icmcb-bordeaux.cnrs.fr; Fax: +33 540 002 761; Tel: +33 540 006 334*
[b]*Institute of Physics, ASCR, Cukrovarnická 10, 162 53 Praha 6, Czech Republic*
[c]*Université de Bordeaux, ENSCBP, 16 avenue Pey Berland, 33607 Pessac Cedex, France*
[d]*CNRS, Laboratoire de Chimie des Polymères Organiques, UMR5629 Pessac, France*

This journal is © The Royal Society of Chemistry 2011

nanoparticles would act not only as heat mediators but also as temperature control switches.

An approach to solve this last task is the use of complex oxides whose magnetic properties may be suitably modified by compositional variations. In this way, perovskites with $La_{1-x}Sr_xMnO_3$ composition (Lanthanum Strontium Manganese Oxide, LSMO) appear to be particularly promising. While the stoichiometric parent compound $LaMnO_3$ is a single-valent (Mn^{3+}) antiferromagnetic insulator,[11] replacement of lanthanum by strontium ions causes a gradual decrease of the steric distortions and the structure changes from the orthorhombic to rhombohedral symmetry. This leads to an insulator–metal transition and, due to predominant Mn^{3+}–O^{2-}–Mn^{4+} double-exchange interactions, to ferromagnetic ordering with a T_C value in the range of 145–371 K, *i.e.* (−132) − 98 °C, for $0.1 \leq x \leq 0.4$.[12]

Few papers dealt with magnetic suspensions based on LSMO or unaggregated LSMO nanoparticles, and some of them were specific for MFH application.[16–21] These nanoparticles were prepared by several routes: the freeze drying technique,[13,14] coprecipitation,[15] Pechini route,[16–18] microwave refluxing technique,[19] and conventional solid-state reactions followed by mechanical milling.[20,21] Nevertheless, each of these techniques necessitate an extra stage of calcination at a temperature over 700 °C in order to get well-crystallized compounds. Therefore, the size distribution of the nanoparticles was large and "connecting bridges" between the individual grains were systematically observed. In order to narrow the size distribution, high-energy mechanical milling and size sorting steps were combined. However, remnant bridges were often maintained leading to the formation of submicrometric aggregates of nanocrystallites.[13–21]

That is why we investigated another route based on the Glycine Nitrate Process (GNP). Among self-combustion synthesis routes, GNP was firstly proposed in 1990 by Chick *et al.* to elaborate chromite and manganite powders.[22] This solution combustion process is particularly suitable for the preparation of multicomponent oxide materials since the homogeneity of the aqueous solution of the metallic salts is preserved in the combustion residue. Moreover it takes advantage of exothermic, fast and self-sustaining chemical reactions between metal nitrates and the glycine reducing agent. As a consequence, it is particularly suited to the elaboration of uniform crystalline particle of ceria[23] or alumina[24] with superfine dimensions. GNP was ever used for the preparation of alkaline earth-doped lanthanum manganite perovskite.[25–30] In general, a molar ratio glycine/nitrate equal to unity was chosen and further calcination appeared systematically necessary to induce crystallinity. Markovic *et al.* reported the GNP synthesis of 10 nm $La_{0.7}Ca_{0.3}MnO_3$ particles without further heating, however, they could not prevent the sponge aspect of the ashes, *i.e.* the agglomeration of crystallites.[28,29]

The success of GNP depends on the correct understanding of the influence of the synthetic parameters. So the main goal of this report is to optimize and validate the suitability of the GNP to prepare easily and efficiently $La_{0.82}Sr_{0.18}MnO_3$ nanoparticles filling the requirements for hyperthermia applications: unaggregated nanoparticles with grain size between 15 nm (to avoid superparamagnetic behavior[28,31,32]) and 100 nm (to prevent any risk of embolization), able to heat in ac magnetic fields and to be coated by a silica layer in order to be easily surface-derivatized for biofunctionalization and stable in aqueous media.[20,33]

Experimental

Synthesis of $La_{0.82}Sr_{0.18}MnO_3$ nanoparticles by GNP

$La_{0.82}Sr_{0.18}MnO_{3+\delta}$ nanoparticles were prepared according to the following protocol. A manganese nitrate solution (1 M) was previously prepared from $Mn(NO_3)_2 \cdot 4H_2O$ (Sigma Aldrich, >97%) dissolved in de-ionised water and titrated by colorimetry. $Mn(NO_3)_2$, $Sr(NO_3)_2$ (Riedel-de Haën, 99%) and $La(NO_3)_3$ (Riedel-de Haën, aqueous solution 0.1 M) were mixed in solution in stoichiometric conditions in order to get 2 g of LSMO (the final volume of solution was about 150 mL). Glycine (Sigma Aldrich, 99%) was dissolved in this solution with various glycine/nitrate molar ratio (G/N) ranging from 0.4 to 1. As-prepared glycine/nitrate solutions were heated on a hot plate (∼400 K) under stirring to evaporate water excess. On further heating (∼520 K), the resulting viscous liquids self-ignited to produce voluminous ashes associated with the emission of large amounts of gases.

In the case where $G/N = 1$, the self-combustion was followed by milling and calcination steps. Ashes (1 g) were introduced in a 45 mL agate bowl with 18 agate balls ($Ø = 10$ mm) and milled in a planetary device (Fritsch-Pulverisette) at 200 rpm during 9 × 30 min (reverse mode). They were then calcinated in an alumina boat into a tubular furnace (rate: 10 K min^{-1}, duration: 2 to 120 min, and temperature: from 973 to 1173 K) and subjected to a second dry milling step including a manual milling (about 15 min in agate mortar) followed by a planetary one with the same experimental conditions as those used before calcination, except the powder mass (∼650 mg) and milling duration (24 × 30 min).

Silica coating

Silica encapsulation process was performed according to a previously reported technique.[34] The surface of the LSMO nanoparticles (1–5 g) was first activated by an acidic treatment (HNO_3, 1 M) in a sonicator bath for 15 min at room temperature. After washing with ultrapure water by several centrifugation cycles, the particles were flocculated by the addition of citric acid (0.01 M), and washed with ultrapure water by centrifugation. Peptization was performed by adding some drops of ammonia on the flakes. Then, the sol of citrated particles was poured into a volume of ethanol/water/ammonia solution 75/23.5/1.5 v/v/v%. To tune the silica shell thickness, the exact amount of tetraethyl orthosilicate (TEOS, Sigma Aldrich) was calculated from the initial and final particle size, taking into account the number of particles N_p, by means of the formula $V_{TEOS} = 3.89 \times N_p \times (D^3 - d^3)$, where V_{TEOS} is directly expressed in mL and D and d are the final and the starting diameters expressed in cm. The 3.89 scaling factor was computed from the molecular weights of SiO_2 formula unit and TEOS, the densities of silica and TEOS (2 and 0.934 g cm^{-3}, respectively) and assuming that particles are spherical. In our case, the silica shell thickness was targeted in the range 4–5 nm. The final step consisted in a size selection of the particles by centrifugation in order to remove residual aggregates.

 This journal is © The Royal Society of Chemistry 2011

Characterization

Elemental analyses were performed by inductively coupled plasma optical emission spectrometry (ICP/OES 720ES Varian). The powder (10 mg) was dissolved in hydrochloric acid (5 mL) and water was added to get 100 mL of solution.

The oxidation state of manganese was determined by standard Mohr's salt titration.[35]

The X-ray diffraction (XRD) patterns were recorded at room temperature on a Philips X'Pert MPD PRO powder diffractometer in the Bragg–Brentano geometry, using Cu-Kα radiations (Kα_1 = 1.54059 Å and Kα_2 = 1.54441 Å). The data collections were made in the 6–80° 2θ range with a 0.02° step. The diffraction data were analyzed using the Fullprof program implementing the Rietveld method.[36] The phase composition analysis was based on data from ICSD.[37] In order to evaluate the mean crystallite size, the Thompson–Cox–Hastings pseudo-Voigt profile was used to resolve the instrumental, strain and size contributions to peak broadening. The instrumental contribution was determined by measuring an home-made standard of LaB_6 with micrometric crystallite size.

The morphology of the nanoparticles was observed by Transmission Electron Microscopy (TEM) on a JEOL JEM 2000FXII apparatus (acceleration voltage 200 kV). A drop of diluted (ethanol) sample was deposited on a carbon-coated copper grid and let to evaporate at room temperature.

ζ Potential experiments were assessed by using a Zetasizer 3000HSA setup (Malvern Instruments) equipped with a He–Ne laser (50 mW, 532 nm). Measurements were performed for 20 s using a standard capillary electrophoresis cell. The dielectric constant of solvent (water) was set to 80.4 and the Smoluchowsky constant f (Ka) was 1.5. The dispersion pH was adjusted in the range 1–11 by adding sodium hydroxide or hydrochloric acid solutions and the isoelectric point was deduced from the titration curve.

The infrared spectra (range 400–4000 cm^{-1}) were measured at room temperature on a FTIR spectrometer (Bruker-Equinox 55) using the DRIFT method. Samples were dried and homogenized (3 wt%) with optically pure KBr.

Static magnetic measurements were carried out on powders by means of a SQUID magnetometer (Quantum Design-MPMS5 XL) between 250 and 350 K up to 4 T. Curie temperatures were evaluated using Arrott plots.

Dynamic light scattering (DLS) analyses were performed with a Cordouan Vasco particle size analyzer set at 20 °C, with a laser wavelength of 650 nm and a static detector set at an angle of 135° from the incident beam. The laser intensity was set to 29% of the maximal power (65 mW) and the correlator parameters *i.e.* time interval and number of channels were set to 10 μs and 300, respectively. All acquisitions were made in multi-acquisition mode on 15 measurements with a time step of 80 s. The particle size distribution was calculated using a Pade–Laplace model, to take into account the nanoparticle polydispersity.

The heating experiments were performed with LSMO suspended in aqueous agarose gel (2.5 wt% of agarose in water) and with LSMO@SiO_2 suspended either in the same agarose gel or in water. The manganese content was 25 g_{Mn} L^{-1} (confirmed by ICP/OEs measurements). Sample suspensions (0.5 mL) were introduced in glass tubes insulated in an expanded polystyrene mantle and placed in a coil connected to a generator (Celes inductor C97104) with a magnetic field amplitude of 88 mT and frequency of 108 kHz.[16] The temperature was monitored by an optical fibre probe (Luxtron STF-2, BFi OPTiLAS SAS).

Results and discussion

Elaboration of LSMO nanoparticles by GNP

In the case of the GNP synthesis of LSMO, the redox combustion reaction is the following:

$$0.82La(NO_3)_3 + 0.18Sr(NO_3)_2 + Mn(NO_3)_2 + nH_2N(CH_2)CO_2H + (2.25n - 5.73)O_2 \rightarrow La_{0.82}Sr_{0.18}MnO_3 + 2nCO_2 + 2.5nH_2O + (2.41 + 0.5n)N_2$$

While the nature of the produced gases is still controversial,[38] propellant chemistry concepts and thermodynamical calculations showed that CO_2, H_2O and N_2 are the most stable products with respect to other theoretically acceptable combinations that might be considered, including the formation of NO_x and CO.[39] For a given fuel, the reaction is governed by the maximum reaction temperature T_m reached during combustion. T_m depends itself on the oxidising/reducing character of the G/N mixture quantified by the so-called φ elemental stoichiometric coefficient. φ is the ratio between the total valencies of fuels and the total valencies of oxidisers, these valencies being considered according to Jain's method.[40] Assigning the +4, +1, +3, +2 and +2 valencies to the C, H, La^{3+}, Sr^{2+} and Mn^{2+} reducing elements, respectively, the −2 valency to O^{2-} oxidizer and considering nitrogen with the valence 0, φ is then calculated according to the following equation:

$$\varphi = \frac{n\left[2 \times 4_{(C)} + 5 \times 1_{(H)} + 0_{(N)} - 2 \times 2_{(O)}\right]}{\left|0.82\left[3_{(La)} + 3\left(0_{(N)} - 3 \times 2_{(O)}\right)\right] + 0.18\left[2_{(Sr)} + 2\left(0_{(N)} - 3 \times 2_{(O)}\right)\right] + \left[2_{(Mn)} + 2\left(0_{(N)} - 3 \times 2_{(O)}\right)\right]\right|}$$

So $\varphi = 9n/24.1$.

The G/N molar ratio (named $G/N = n/4.82$) is then equal to $[(24.1\varphi/9)/4.82]$ so 0.56φ. The reaction is considered stoichiometric when the total valency of reducing elements balances the valency of oxidizing ones. In this case, $\varphi_{stoichio}$ is equal to 1 which involves $n_{stoichio}$ equal to 2.68 and $G/N_{stoichio}$ equal to 0.56. The conditions are called oxidant-rich for $\varphi < 1$ and fuel-rich for $\varphi > 1$.

Attempted synthesis in a single step

Our first strategy was to synthesize perovskite nanoparticles in a single step to avoid any further calcination and therefore limit

particles sintering. We studied the influence of the *G*/*N* ratio on the purity and size of the particles of as-synthesized materials. Whatever the *G*/*N* ratio, GNP led to black ashes.

Fig. 1 shows XRD patterns for manganite perovskite prepared with *G*/*N* values ranging from 0.4 to 0.7 (φ = 0.72–1.26, *i.e.* volume combustion regime[41]). Whatever the *G*/*N* ratio, the major phase corresponded to the well-defined perovskite structure with rhombohedral symmetry described in an hexagonal cell, all peaks being fully indexed in $R\bar{3}c$ space group. The peak widths were consistent with nanosized crystallites. However, some impurities systematically appeared and could be classified as follows: (i) $SrCO_3$, $Sr(NO_3)_2$ and $LaO(NO_3)$ in decreasing amounts when the *G*/*N* value was increased and (ii) carbonaceous residue (main peak centered around 30° (2θ)) when *G*/*N* ratio was in the range 0.6–0.7 and in amounts all the more important since the *G*/*N* value was increased. The presence of such a carbonaceous residue was previously reported in fuel-rich conditions.[39]

In this way, the synthesis must be considered regarding both fundamental aspects which are influenced by the *G*/*N* ratio. On the one hand, the *G*/*N* ratio directly influences the chelation of metallic cations. If the amount of glycine is not sufficient, the cations are not fully chelated; the un-chelated nitrates then crystallize during heating and evaporation which explains the formation of cation-based impurities.[27] Then, as the *G*/*N* ratio increases, cations are more and more chelated, however, even for *G*/*N* equal to 0.7 (φ = 1.26), some cations still remain uncomplexed. Moreover, because the impurities are mainly lanthanum and strontium-based compounds, one should deduce that glycine preferentially chelates manganese ions. Nevertheless Chick *et al.*[22] and Peng *et al.*[27] claimed a preferential chelation of the manganese ions by amine function. One should remember that pK_a of amine and carboxyl functions are 9.6 and 2.3, respectively, while the pH of the solution before heating is 4.8. In these conditions, glycine is then present as a zwitterion NH_3^+–CH_2–COO^- and carboxyl function is the only one available to chelate cations. The chemical nature of impurities tends then to evidence a preferential chelation of manganese in these pH conditions. If pH is increased above 9.6, amine function can become efficient for chelation but these basic conditions can favour hydroxide precipitation. On the other hand, *G*/*N* ratio strongly influences the maximum reaction temperature T_m: when φ (thus *G*/*N*) increases, T_m first increases until $\varphi = 1$ stoichiometric conditions are reached and then decreased in fuel-rich conditions because large amounts of gases (CO_2, H_2O, N_2) are released which dissipates the heat of the process. As a consequence, for the highest *G*/*N* values, the released energy was not sufficient to burn all the organic matter and that is why a carbonaceous residue was observed.

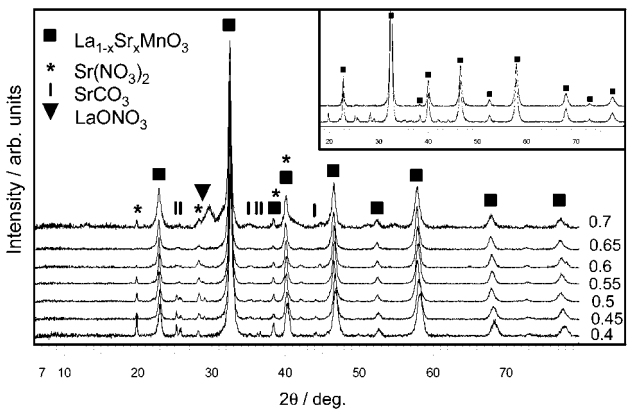

Fig. 1 XRD patterns of LSMO obtained by single step GNP for *G*/*N* (values on the right) ranging from 0.4 to 0.7. Main reflexions of impurities are marked. In the inset, XRD pattern for *G*/*N* = 0.5 before (bottom) and after (top) acidic washing.

Whatever their chemical nature and for any *G*/*N* value, all impurities were removed from the samples thanks to an acidic washing (see the inset in Fig. 1 as an example). Then, on the whole *G*/*N* range, we succeeded in characterizing pure perovskite materials. Chemical compositions of washed samples are given in Table 1. It may be observed that, as expected, whatever the *G*/*N* value, the samples are highly strontium- and lanthanum-deficient.

Stoichiometric conditions tend to favour perovskite formation as, in this case, average occupation rate on A site is maximum ($0.55 \leq G/N \leq 0.60$). For the lower *G*/*N* values, chelation was insufficient and A-cations were partially involved in the formation of impurities as ever discussed. For the higher *G*/*N* values, chelation was better, but T_m drastically decreased and became insufficient to burn the whole organic matter, some A-cations being then trapped into this organic residue.

Despite an almost constant cationic composition, *a* and *c* parameters of the washed samples strongly increased with the *G*/*N* value (Fig. 2). The slight modulations of composition on A site could not be responsible for these variations as the average cationic radius on this site was constant while its average occupation rate did not evolve on a monotonous way. When the *G*/*N* ratio was increased, the relative nitrate amount decreased, then the oxidizing power decreased too. As a consequence, a reduction of manganese oxidation state should have been observed. The decrease of Mn^{4+} shown in Table 1 becomes more important with increasing *G*/*N* ratio. Then, because Mn^{3+} ion is much more bigger than Mn^{4+} ion, the cell parameters increase with *G*/*N*.

The evolution of the crystallite size as a function of the *G*/*N* is presented in Fig. 3. Crystallites exhibited mostly sizes lower than 20 nm which were in accordance with the required specifications for MFH. One should notice that this crystallite size logically evolved as T_m as a function of *G*/*N*, the maximum size (~20 nm) being obtained for the highest T_m when the reaction was stoichiometric.[23,24,43]

The single-step GNP synthesis allowed us to successfully elaborate some crystallized perovskite nanoparticles.

Table 1 Cationic ratios, average cationic sizes on A (R_{Amean}, La^{3+}/Sr^{2+}) and B (R_{Bmean}, Mn^{4+}/Mn^{3+}) sites, average occupation rate on A site[a] and amount of Mn^{4+} as a function of *G*/*N* value. Ionic radii of $La^{3+}_{(XII)}$, $Sr^{2+}_{(XII)}$, $Mn^{4+}_{(VI)}$ and $Mn^{3+}_{(VI)}$ are 1.36, 1.44, 0.53 and 0.645 Å, respectively[42]

G/*N*	0.4	0.45	0.5	0.55	0.6	0.65	0.7
La/Mn	0.67	0.70	0.69	0.72	0.72	0.66	0.66
Sr/Mn	0.04	0.06	0.04	0.05	0.08	0.04	0.04
% Occ_A	71	76	73	77	80	70	70
R_{Amean}/Å	1.364	1.366	1.364	1.365	1.364	1.362	1.362
% Mn^{4+}	21			10		8	
R_{Bmean}/Å	0.621			0.634		0.636	

[a] % Occ_A was calculated from cationic ratios considering that Mn-B site was fully occupied.

This journal is © The Royal Society of Chemistry 2011

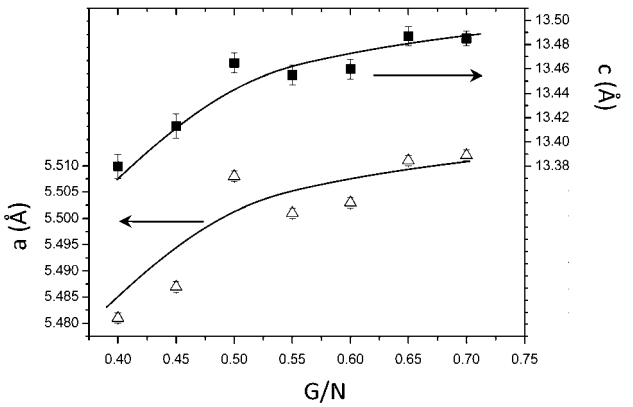

Fig. 2 Evolution of the hexagonal cell parameters *a* and *c* of LSMO *vs. G*/*N* values (samples after washing, without calcination). Solid lines are just guide-to-the-eye.

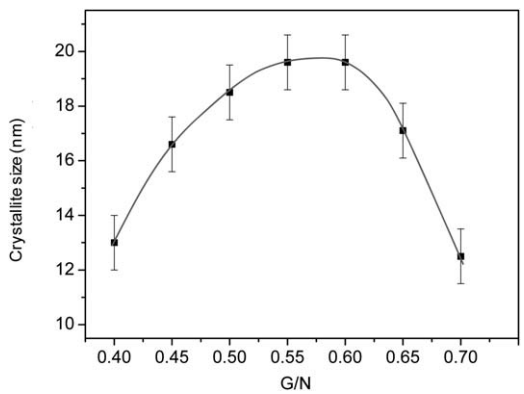

Fig. 3 Evolution of the crystallite size as determined by XRD of LSMO *vs. G*/*N* (samples after washing, without calcination). Solid line is just guide-to-the-eye.

Nevertheless, this strategy was not convenient because the chelation was clearly incomplete and consequently lanthanum and strontium were inserted only partly into the perovskite structure. Therefore, all the materials were paramagnetic at room temperature and thus unsuitable for self-controlled MFH application.

It appeared crucial to increase the glycine amount (thus φ) in order to improve the metal chelation. On the one hand this increase of φ involved a more affluent gas release which could prevent the formation of sintering bridges between particles; as a consequence, the formation of nanosized unagglomerated particles could be favoured. However, on the other hand, increasing φ would necessarily decrease T_m, which implied a poor crystallinity of the materials and an increase of carbonaceous residue. Therefore, a further calcination stage then appeared unavoidable.

GNP synthesis combining an extra step of calcination

The *G*/*N* ratio was chosen equal to 1 (so $\varphi = 1.8$, *i.e.* fuel-rich self-sustained combustion regime[41,44]) in order to reach an efficient improvement of chelation without any drastic alteration of particles crystallinity. As expected, the ashes obtained after GNP synthesis with $G/N = 1$ consisted in a poorly crystallized perovskite with a carbonaceous residue as an impurity (an example is given in Fig. 4A). No trace of inorganic parasitic phase was detected.

Whatever the used calcination temperature T_{calc} and its duration D_{calc} (ranging from 973 to 1173 K and 2 to 120 min, respectively), well crystallized single phase manganese perovskites were obtained after the thermal treatment of the ashes (an example is given in Fig. 4B). ICP-OES characterization confirmed the accordance of cationic molar ratios with targeted values La/Mn = 0.82(2); Sr/Mn = 0.18(2) whatever be the couple (T_{calc}, D_{calc}). The evolutions of crystallite sizes as a function of T_{calc} and D_{calc} are demonstrated in Fig. 5. For the lowest T_{calc}, the curve can be described as follows: after a rapid increase more important for a higher T_{calc}, the crystallite sizes reached a plateau at a value all the more great since T_{calc} was raised (roughly 11 and 14 nm at 973 and 1023 K, respectively). However it is obvious that the calcination at 1023 K or at lower temperatures will not allow us to get sufficient crystallite sizes even after longest durations. The achieved maximum of 14 nm is lower than our specifications (15 nm to avoid superparamagnetism).[28,31,32] One could expect the same crystallite size *vs.* time tendencies for 1073 and 1173 K, however, the experiment durations were too short to observe the plateau. Sizes obtained at 1173 K (even for shorter durations) were in accordance with the MFH requirements, however, at this temperature sintering was widely promoted and strong grain boundaries were formed between particles as evidenced on Fig. 6A. Fig. 6B confirms that after a calcination at 1073 K for 30 min particles were nanosized (average size < 100 nm) but it also evidences that some more thin connecting bridges were present between the particles. Therefore the calcination conditions of 1073 K and annealing time of 30 min were selected for upcoming experiments.

Then, in order to improve their desaggregation, the conditions of the milling step were optimized. Many experiments were attempted changing either the milling process (ball milling, rolling), milling duration or the size and number of balls (in the case of the ball milling), *etc.* The material remained unchanged when milling conditions were not sufficiently energetical. In contrast, if the milling energy was too high, *e.g.* by using of the 8000M Spex ball mixer mill, the size and crystallinity of nanoparticles were strongly affected (as an example can serve a decrease of the crystallite size from 22 nm down to 9 nm

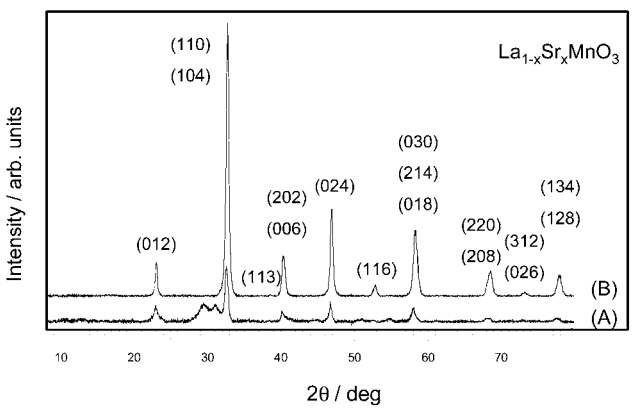

Fig. 4 XRD pattern of LSMO sample after GNP synthesis for $G/N = 1$, (A) without calcination and (B) after calcination at 1173 K for 2 min.

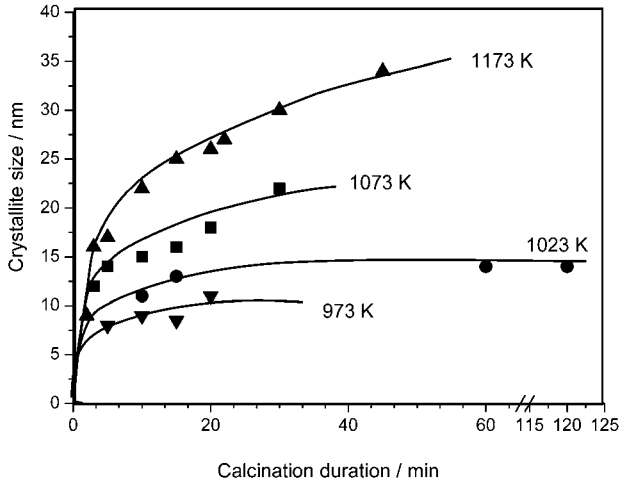

Fig. 5 Influence of the temperature and duration of calcination on the crystallite size of LSMO ($G/N = 1$). Solid lines are just guide-to-the-eye.

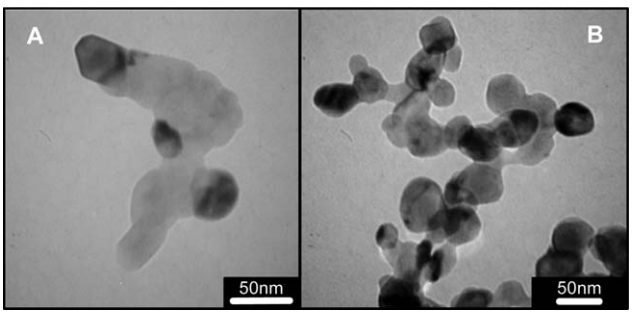

Fig. 6 TEM images of LSMO nanoparticles as a function of calcination temperature and duration: (A) 1173 K, 20 min; and (B) 1073 K, 30 min.

observed by XRD and TEM). Our best results were obtained by two steps procedure employing planetary ball mill. The first step (see Experimental part) was performed on the ashes, *i.e.* before the calcination, and served to break the sponge morphology and to nullify the nascent sintering bridges. The second step was processed after the calcination under elevated energetical conditions (see Experimental part).

The particles obtained using such a protocol will be named "optimized" particles. ICP-OES characterization confirmed unchanged cationic ratios after milling. Moreover, XRD characterization of the optimized particles evidenced the preserved original crystallite size (22 nm). It confirms that the second milling step affects only the sintering bridges and not the nanoparticles themselves.

Finally redox titration was performed on optimized particles and the deduced oxidation state of manganese was found to be $Mn^{3.36+}$ (36% Mn^{4+}). It was then obvious that the oxidation state of manganese deviated from the theoretical one ($Mn^{3.18+}$ considering that the material is perfectly stoichiometric both on the cationic and anionic sites). However, this result was not unexpected as calcination conditions were significantly oxidizing in comparison to those required to get stoichiometric compounds. This oxidation phenomenon induced by the synthesis shall be carefully considered when studying the hyperthermia behavior of magnetic fluids based on these magnetic cores.

From manganite nanoparticles to hyperthermia mediators

Silica coating. Because the MFH application requires the use of a stable colloidal suspension of surface-functionalizable nanoparticles, the optimized manganite nanoparticles were individually encapsulated in a silica shell[33] leading to the core@shell particles (LSMO@SiO_2). The coating process was derived from the Stöber's method using tetraethoxysilane (TEOS) in highly polar mixtures of ethanol and water alkalized by ammonia.[45,46]

After coating, the LSMO crystallite size was determined by XRD and was found to be unchanged during encapsulation process (22 nm). A comparison of IR spectra of particles before (Fig. 7A) and after encapsulation process (Fig. 7B) unambiguously confirmed the silica formation. Fig. 7B shows all the typical bands of amorphous silica that are not observed on uncoated particle spectrum (Fig. 7A). The band at 1100 and 800 cm^{-1} corresponds to asymmetric and symmetric stretching vibration of Si–O–Si, respectively. The bending vibration of Si–O–Si induces a local maximum at 475 cm^{-1} while that of Si–OH manifests itself at 950 cm^{-1}, hence revealing the presence of silanol groups. Moreover, the band centered at 640 cm^{-1} appears on both spectra and is related to the inorganic manganite core as it is assigned to Mn–O–Mn symmetric stretching vibrations.[47,48] Because it is clearly visible on the spectrum of coated particles, one should deduce that the silica shell, if present, is rather thin as for higher thickness (20 nm) a shielding effect tends to make this band disappear.[33]

Silica coating was also evidenced by studying the dependence of the ζ potential with pH (Fig. 8). The isoelectric point (IEP) shifts from pH 7 for uncoated particles (Fig. 8A) down to pH 3.7 after silica coating (Fig. 8B). IEP was expected between pH 2 and 3 for silica.[49] The observed shift was probably due to the partial dissolution in acidic pH of cations at the surface of LSMO nanoparticles, silica coating being porous and thin enough to allow their diffusion; these cations then acted as a potential determining ion.[50] One should also notice that a single value of ζ potential was measured for each pH value which certified that sample could not be considered as a mixture of LSMO particles with silica ones.

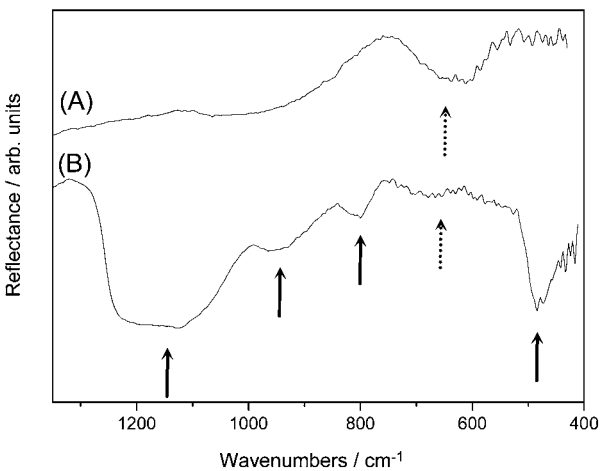

Fig. 7 IR spectra of (A) LSMO and (B) LSMO@silica particles. Solid and dotted arrows point bands of silica and LSMO, respectively.

This journal is © The Royal Society of Chemistry 2011

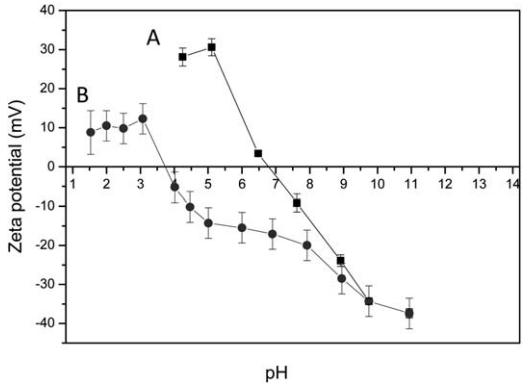

Fig. 8 ζ Potential measurements *vs.* pH for aqueous dispersions of (A) LSMO and (B) LSMO@silica nanoparticles.

Coated particles were also characterized by TEM experiments (Fig. 9). One should first notice that the coating was satisfactorily uniform, with a silica thickness of about 5 nm. The average particles size ranged between 20 and 100 nm with more numerous particles around 50–70 nm which is in agreement with the required specifications. The hydrodynamic diameter of coated nanoparticles was finally characterized by DLS (Fig. 10). The main peak was centered on 100 nm which is consistent with TEM image (Fig. 9). Moreover, one should observe the absence of large aggregates.

Magnetic fluid hyperthermia performances of the optimized material

Both uncoated and silica coated optimized $La_{0.82}Sr_{0.18}MnO_3$ nanoparticles exhibited a ferromagnetic behavior at room temperature. T_C of both samples was measured according to the Arrott's method (Fig. 11). In both cases, T_C was found to be equal to 316 K which confirmed that the silica coating process did not significantly modify the inorganic core. This T_C value was far from the expected one for stoichiometric material (288 K for $La_{0.82}Sr_{0.18}MnO_3$ (ref. 12)). In our case, one should remember that the material contains 36% Mn^{4+} instead of theoretical 18%. If the anionic network is considered fully occupied, the deduced chemical composition is then

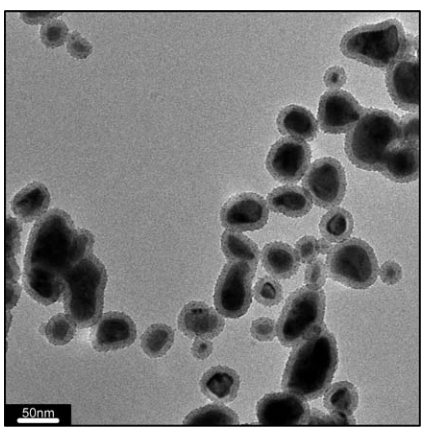

Fig. 9 TEM image of silica-coated LSMO particles.

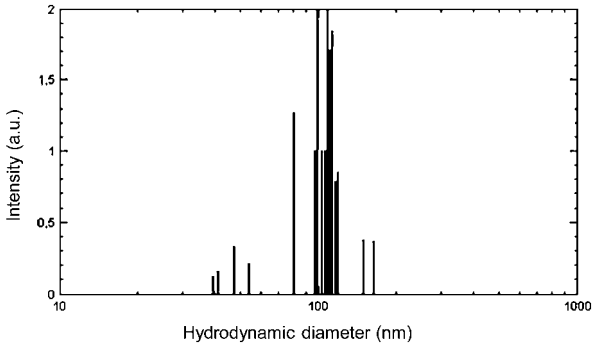

Fig. 10 DLS histogram LMSO@silica nanoparticles.

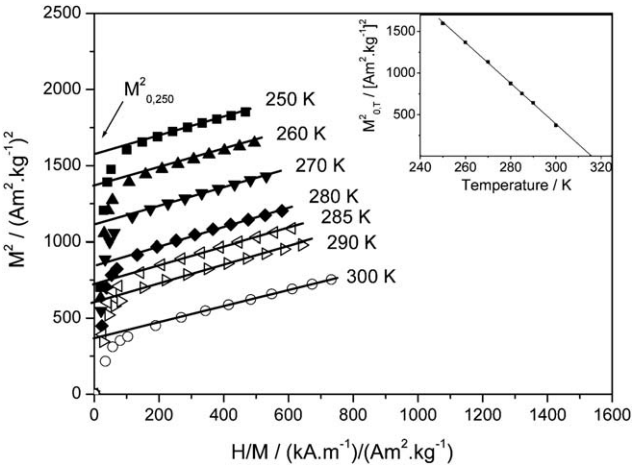

Fig. 11 Determination of T_C of uncoated LSMO particles according to the Arrott's method. The evolution of M^2 *vs.* H/M at a given temperature T is deduced from magnetic hysteresis at T. The linear regression of the upper part leads to $M^2_{0,T}$, the intercept with Y-axis at T. The curve $M^2_{0,T}$ *vs.* T (inset) is then a straight line which intercepts with X-axis at T_C.

$(La_{0.82}Sr_{0.18})_{0.97}(Mn^{3+}{}_{0.64}Mn^{4+}{}_{0.36})_{0.97}O_3$. In this case, T_C increase reveals a significant enhancement of the double exchange interactions which do not suffer from 3% vacancies on the manganese site. A same tendency was ever observed in $La_{1-x}MnO_3$ where antiferromagnetism (stoichiometric sample with dominant superexchange interactions) turned to ferromagnetism when increasing x due to an increasing of the oxidation state of manganese which favoured ferromagnetic double exchange interactions.[51] We believe that, in the present case, the evolution of T_C is due to the chemical influences rather than of the size effects.[52]

The magnetic heating experiments carried out both on coated and uncoated LSMO particles, suspended either in water or agarose gel, revealed heating temperature T_{heat} *vs.* time dependences characterized by a sharp onset of T_{heat} followed by its stabilization at a maximum $T_{heat\ max}$ (Fig. 12). First of all, one should notice that, whatever the dispersion medium, the heating behavior was unchanged which confirmed that heating originated from hysteresis losses rather than Brownian rotation because agarose is known to prevent any motion of the particles[53] (Fig. 12B and C). Moreover, it was remarkable that $T_{heat\ max}$ (315–316 K, *i.e.* 42–43 °C) reached T_C for coated and uncoated particles. As expected, manganite nanoparticles both act as

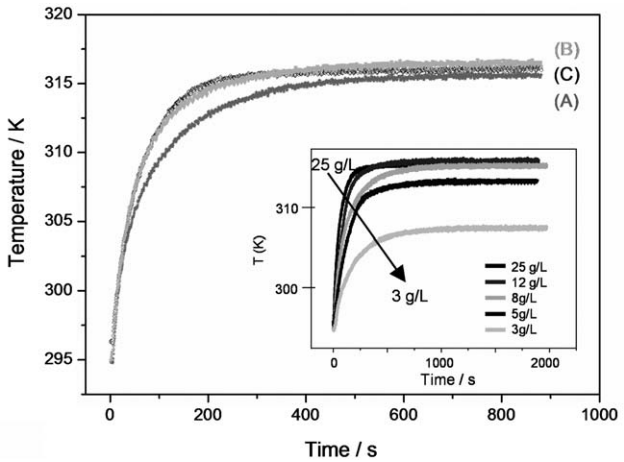

Fig. 12 Magnetic heating experiments ([Mn] = 25 g L^{-1}; ac field conditions: 88 mT, 108 kHz) for (A) LSMO in agarose, (B) LSMO@silica in agarose, and (C) LSMO@silica in water. In the inset: magnetic heating experiments for LSMO (88 mT, 108 kHz) *vs.* manganese concentration.

a heater and a fuse as they stop heating when reaching their paramagnetic state. In this way, $T_{\text{heat max}}$ will never exceed T_C. However, when manganese concentration decreased below 8 g L^{-1}, there were not enough particles to heat the whole system and the temperature stabilisation originated from the unsufficiently insulated calorimetry device. The main difference observed concerned the heating efficiency evaluated from the calculation of the specific absorption rate SAR, defined as:

$$\text{SAR} = C_P/w_{\text{Mn}} \times \text{d}T/\text{d}t$$

where C_P was the specific heat capacity of the sample (equivalent for water and aqueous agarose gel[33]) under constant pressure, w_{Mn} was the weight fraction of the magnetically active element and dT/dt the derivative of the slope T_{heat} *vs.* time. It was obvious that the values of SAR at 310 K (37 °C, *i.e.* body temperature) showed higher heating efficiency for silica-coated particles (SAR = 16 W g^{-1}) rather than for uncoated ones (SAR = 9.6 W g^{-1}). The same tendency has ever been encountered in the literature where it was claimed that heating efficiency is all the more enhanced since nanoparticles are efficiently dispersed.[33,54] In the present case, the dispersion of uncoated particles in agarose was less efficient in particular because the size selection had not been performed in this case. Therefore, some residual aggregates were probably present and the dispersion was far from an optimum. However, some further studies should be necessary to corroborate this hypothesis.

However, these preliminary heating experiments were really promising because the maximum heating temperature was fully in agreement with MFH requirements.

Conclusion

A smart reproducible procedure of the preparation of well-separated core@shell particles was developed and optimized. GNP was an adequate route to elaborate nanosized inorganic $La_{0.82}Sr_{0.18}MnO_{3+\delta}$ cores. Best synthesis conditions were found in the fuel-rich self-sustained combustion regime where chelation was widely enhanced. Consequently, because such conditions led to a significant decrease of the maximum combustion reaction temperature, a further fast calcination step was mandatory to improve crystallinity and remove organic residues. Moreover, this thermal treatment appeared necessary in order to control the mixed valency of manganese upon which T_C depends. Efficient desaggregation was then performed by a two-step planetary milling process to destroy nascent sintering effects. Such particles were successfully encapsulated by a controlled-in-thickness 5 nm silica shell employing a procedure derived from the Stöber method. After whole process, no aggregate was detected and nanoparticles got a size and a heating behavior in agreement with MFH requirements. Further experiments are in progress in order to check their biocompatibility, before their surface bio-functionalisation and *in vivo* evaluation.

Acknowledgements

S. Gomez is gratefully acknowledged for TEM experiments (CREMEM, Talence, France). R. Epherre was supported by a grant from Le Conseil Régional d'Aquitaine. This work was performed in the framework of the FAME FP6 European Network of Excellence and the project NanoBioImaging of the Agence Nationale pour la Recherche. It was also supported through the CPER Pôle 4N Nanosciences en Aquitaine (GP 206-action 216/1) by the Conseil Régional d'Aquitaine, FEDER, CNRS and Ministère de l'Enseignement Supérieur et de la Recherche.

References

1 A. Jordan, R. Scholz, K. Maier-Hauff, M. Johanssen, P. Wust, J. Nadobny, H. Schmidt, S. Deger, S. Loening, W. Lanksch and R. Felix, *J. Magn. Magn. Mater.*, 2001, **225**, 118.
2 M. H. Falk and R. D. Issels, *Int. J. Hyperthermia*, 2001, **17**, 1.
3 I. Hilger, A. Kiessling, E. Romanus, R. Hiergeist, H. T. Rudolf, W. Andrä, M. Roskos, W. Linss, P. Weber, W. Weitshies and W. A. Kaiser, *Nanotechnology*, 2004, **15**, 1027.
4 E. Duguet, S. Mornet, S. Vasseur and J. M. Devoisselle, *Nanomedicine*, 2006, **1**, 157.
5 S. Laurent, D. Forge, M. Port, A. Roch, C. Robic, L. Vander Elst and R. N. Muller, *Chem. Rev.*, 2008, **108**, 2064.
6 Q. A. Pankhurst, N. K. T. Thanh, S. K. Jones and J. Dobson, *J. Phys. D: Appl. Phys.*, 2009, **42**, 224001(15pp).
7 C. Corot, P. Robert, J. M. Idée and M. Port, *Adv. Drug Delivery Rev.*, 2006, **58**, 1471.
8 M. Johannsen, U. Gneveckow, B. Thiesen, K. Taymoorian, C. H. Cho, N. Waldöfner, R. Scholz, A. Jordan, S. A. Loening and P. Wust, *Eur. Urol.*, 2007, **52**, 1653.
9 B. Thiesen and A. Jordan, *Int. J. Hyperthermia*, 2008, **24**, 467.
10 A. Jordan and K. Maier-Hauff, *J. Nanosci. Nanotechnol.*, 2007, **7**, 4604.
11 E. Wollan and W. Koehler, *Phys. Rev.*, 1955, **100**, 545.
12 A. Urushibara, Y. Moritomo, T. Arima, A. Asamitsu, G. Kido and Y. Tokura, *Phys. Rev. B: Condens. Matter*, 1995, **51**, 14103.
13 A. A. Kuznetsov, O. A. Shlyakhtin, N. A. Brusentsov and Q. A. Kuznetsov, *Eur. Cells Mater.*, 2002, **13**, 75.
14 Y. Koksharov, V. Nikiforov, V. Kuznetsov and G. Khomutov, *Microelectron. Eng.*, 2005, **81**, 371.
15 V. Uskokovic and M. Drofenic, *Mater. Des.*, 2007, **28**, 667.
16 S. Vasseur, E. Duguet, J. Portier, G. Goglio, S. Mornet, E. Hadová, K. Knížek, M. Maryško, P. Veverka and E. Pollert, *J. Magn. Magn. Mater.*, 2006, **302**, 315.
17 E. Pollert, K. Knizek, M. Marysko, P. Kaspar, S. Vasseur and E. Duguet, *J. Magn. Magn. Mater.*, 2007, **316**, 122.
18 N. X. Phuc, N. A. Tuan, N. C. Thuan, V. A. Tuan and L. V. Long, *Adv. Mater. Res.*, 2008, **55–57**, 27.

 This journal is © The Royal Society of Chemistry 2011

19 N. K. Prasad, K. Rathinasamy, D. Panda and D. Bahadur, *J. Biomed. Mater. Res., Part B*, 2008, **85**, 409.
20 V. Uskoković, A. Košak and M. Drofenik, *Mater. Lett.*, 2006, **60**, 2620.
21 A. Villanueva, P. de la Presa, J. M. Alonso, T. Rueda, A. Martinez, P. Crespo, M. P. Morales, M. A. Gonzalez-Fernandez, J. Valdes and G. Rivero, *J. Phys. Chem. C*, 2010, **114**, 1976.
22 L. A. Chick, L. R. Pederson, G. D. Maupin, J. L. Bates, L. E. Thomas and G. J. Exarhos, *Mater. Lett.*, 1990, **10**, 6.
23 R. D. Purohit, B. P. Sharma, K. T. Pillai and A. K. Tyagi, *Mater. Res. Bull.*, 2001, **36**, 2711.
24 J. C. Toniolo, M. D. Lima, A. S. Takimi and C. P. Bergmann, *Mater. Res. Bull.*, 2005, **40**, 561.
25 L. Da Conceição, N. F. P. Ribeiro, J. G. M. Furtado and M. M. V. M. Souza, *Ceram. Int.*, 2009, **35**, 1683.
26 C. Yang, A. Coffin and F. Chen, *Int. J. Hydrogen Energy*, 2010, **35**, 3221.
27 R. Peng, X. Fan, Z. Jiang and C. Xia, *Fuel Cells*, 2006, **6**, 455.
28 D. Markovic, V. Kusigerski, M. Tadic, J. Blanusa, M. V. Antisari and V. Spasojevic, *Scr. Mater.*, 2008, **59**, 35.
29 D. Markovic, V. Kusigerski, M. Tadic, J. Blanusa, Z. Jaglicic, N. Cvjeticanin and V. Spasojevic, *J. Alloys Compd.*, 2010, **494**, 52.
30 D. Berger, C. Matei, F. Papa, D. Macovei, V. Fruth and J. P. Deloume, *J. Eur. Ceram. Soc.*, 2007, **27**, 4395.
31 A. Rostamnejadi, H. Salamati, P. Kameli and H. Ahmadvand, *J. Magn. Magn. Mater.*, 2009, **321**, 3126.
32 P. Dey and T. K. Nath, *Appl. Phys. Lett.*, 2006, **89**, 163102.
33 O. Kaman, E. Pollert, P. Veverka, M. Veverka, E. Hadová, K. Knížek, M. Maryško, P. Kašpar, M. Klementová, V. Grünwaldová, S. Vasseur, R. Epherre, S. Mornet, G. Goglio and E. Duguet, *Nanotechnology*, 2009, **20**, 275610.
34 S. Mornet, C. Elissalde, O. Bidault, F. Weill, E. Sellier, O. Nguyen and M. Maglione, *Chem. Mater.*, 2007, **19**, 987.
35 A. Wattiaux, J. C. Grenier, M. Pouchard and P. Hagenmuller, *J. Electrochem. Soc.*, 1997, **134**, 1714.
36 J. Rodriguez-Carvajal, *Fullprof.2k Version 4.30*, ILL JRC, April 2008.
37 *Inorganic Crystal Structure Database, Version 2008*, National Institute of Standards and Technology (NIST) and Fachinformationszentrum Karlsruhe (FIZ), 2008.
38 T. Pine, X. Lu, D. R. Mumm, G. S. Samuelsen and J. Brouwer, *J. Am. Ceram. Soc.*, 2007, **90**, 3735.
39 A. Civera, M. Pavese, G. Saracco and V. Specchia, *Catal. Today*, 2003, **83**, 199.
40 S. R. Jain, K. C. Adiga and V. R. P. Verneker, *Combust. Flame*, 1981, **40**, 71.
41 K. Desphande, A. Mukasyan and A. Varma, *J. Am. Ceram. Soc.*, 2003, **86**, 1149.
42 R. D. Shannon and C. T. Prewitt, *Acta Crystallogr., Sect. B: Struct. Crystallogr. Cryst.Chem.*, 1969, **25**, 925.
43 X. Pingbo, Z. Weiping, Y. Kuo, J. Long, Z. Weiwei and X. Shangda, *J. Alloys Compd.*, 2000, **311**, 90.
44 M. T. Caldes, G. Goglio, C. Marhic, O. Joubert, M. Lancin and L. Brohan, *Int. J. Inorg. Mater.*, 2001, **3**, 1169.
45 S. Mornet, C. Elissalde, V. Hornebecq, O. Bidault, E. Duguet, A. Brisson and M. Maglione, *Chem. Mater.*, 2005, **17**, 4530.
46 W. Stöber, A. Fink and E. Bohn, *J. Colloid Interface Sci.*, 1968, **26**, 62.
47 X. Wang, Q. Cui, Y. Pan and G. Zou, *J. Alloys Compd.*, 2003, **354**, 91.
48 K. Li, R. Cheng, S. Wang and Y. Zhang, *J. Phys.: Condens. Matter*, 1998, **10**, 4315.
49 Z. Wu, H. Xiang, T. Kim, M. S. Chun and K. Lee, *J. Colloid Interface Sci.*, 2006, **304**, 119.
50 R. J. Hunter, *Foundations of Colloid Science*, Elsevier, 2001.
51 V. Ferris, G. Goglio, L. Brohan, O. Joubert, P. Molinié, M. Ganne and P. Dordor, *Mater. Res. Bull.*, 1997, **32**, 763.
52 R. Epherre, G. Goglio, *et al.*, unpublished results.
53 R. Hiergeist, W. Andrä, N. Buske, R. Hergt, I. Hilger, U. Richter and W. Kaiser, *J. Magn. Magn. Mater.*, 1999, **201**, 420.
54 D. H. Kim, D. E. Nikles, D. T. Johnson and C. S. Brazel, *J. Magn. Magn. Mater.*, 2008, **320**, 2390.